Macromolecules

pubs.acs.org/Macromolecules

Article

Chemical Feedback in Templated Reaction-Assembly Networks

Inge Bos, Camilla Terenzi, and Joris Sprakel*

Cite This: *Macromolecules* 2020, 53, 10675−10685

Read Online

ACCESS | Metrics & More | Article Recommendations | Supporting Information

ABSTRACT: Chemical feedback between building block synthesis and their subsequent supramolecular self-assembly into nanostructures has profound effects on assembly pathways. Nature harnesses feedback in reaction-assembly networks in a variety of scenarios including virion formation and protein folding. Also in nanomaterial synthesis, reaction-assembly networks have emerged as a promising control strategy to regulate assembly processes. Yet, how chemical feedback affects the fundamental pathways of structure formation remains unclear. Here, we unravel the pathways of a templated reaction-assembly network that couples a covalent polymerization to an electrostatic coassembly process. We show how the supramolecular staging of building blocks at a macromolecular template can accelerate the polymerization reaction and prevent the formation of kinetically trapped structures inherent to the process in the absence of feedback. Finally, we establish a predictive kinetic reaction model that quantitatively describes the pathways underlying these reaction-assembly networks. Our results shed light on the fundamental mechanisms by which chemical feedback can steer self-assembly reactions and can be used to rationally design new nanostructures.

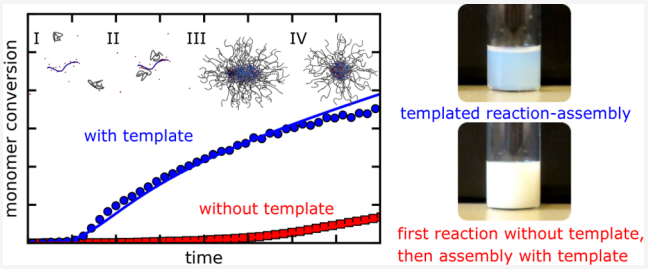

INTRODUCTION

In nature, the biosynthesis of macromolecular building blocks and their assembly often occur simultaneously and within the same cellular compartment.[1−4] The spatiotemporal colocalization of covalent and supramolecular reactions, involving the same molecular compounds, results in feedback between the different primary chemical reactions. Chemical feedback in these coupled reaction-assembly networks has profound effects on both the kinetics of the process and the final products that the coupled reactions yield. For example, the structure of virions is different when the translation of viral coat proteins occurs simultaneously with the DNA-templated assembly process as compared to the case when all proteins are already present at the start of the assembly.[3,5,6] Also in protein biosynthesis itself, folding of the polypeptide chain into the desired tertiary structure can be regulated by the rate of its translation.[4,7]

Supramolecular assembly strategies have become a paradigm in the creation of a plethora of synthetic nanomaterials.[8−11] However, while in nature reaction and assembly are invariably coupled, for synthetic materials the synthesis of the building blocks and their subsequent self- or coassembly have traditionally been separated in both space and time. This facilitates experimental control on the purity and characterization of the building blocks and of the details of the assembly process, but it also limits the structures than can be made, and the pathways by which these are reached, as the covalent reaction cannot be used to tune the assembly. In recent years, interest in the use of coupled reaction-assembly processes has emerged as a control mechanisms for creating synthetic nanomaterials. A seminal example is polymerization-induced self-assembly (PISA), in which covalent polymerizations of amphiphilic macromolecules are coupled to the formation of micellar and vesicular structures that could not have been created using the classical spatiotemporal separation of the covalent and supramolecular processes.[12] Many examples of this strategy have now been reported.[13−15] More recently, this approach has been extended to templated assembly reactions. In polymerization-induced electrostatic self-assembly (PIESA), the polymerization of a polyelectrolyte occurs in the presence of oppositely charged macroions that serve as a molecular template for the assembly.[16−20] This is of particular interest because templated assembly, in which a macromolecular template acts as a blueprint for the assembly process, is a common approach used by nature to guide multicomponent systems across their complex supramolecular energy landscapes to the desired final structure.[21−23] Yet, the control of templated assembly in the synthetic realm remains challenging.[24]

Despite the promise of these templated reaction-assembly networks, mechanistic insights into the emergence of chemical feedback in these networks remain elusive. For example, it is unclear how the kinetic pathways across underlying elementary reaction steps are affected by the coupling. Moreover, comprehensive and predictive models that capture the essence

Received: August 18, 2020
Revised: November 2, 2020
Published: November 23, 2020

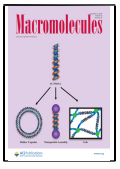

https://dx.doi.org/10.1021/acs.macromol.0c01915
Macromolecules 2020, 53, 10675−10685

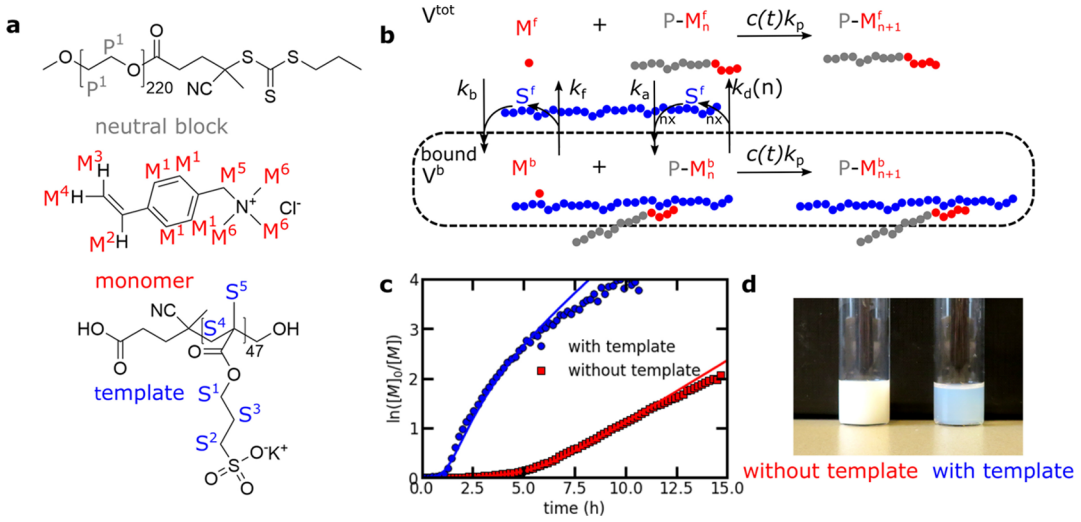

Figure 1. Templated reaction-assembly network. (a) Different components of the network. (b) Schematic overview of the templated reaction-assembly network and simplified representation of the kinetic model. (c) Pseudo-first-order kinetic plot of the polymerization reaction with and without the template. Solid lines indicate kinetic model predictions for the polymerization with the template $k_p = 0.36\ mM^{-1}\ h^{-1}$, $k_b = k_a = 12\ mM^{-1}\ h^{-1}$, $k_{bn} = 500k_b$, $k_d(n) = \omega_0 \exp(-nE_a/k_BT)$ with $\omega_0 = 3.1 \times 10^4\ h^{-1}$, and $E_a = 6k_BT$, $k_f = k_d(1)$, $V^{tot}/V^b = 8$, $a = 3.0$, $t_{shift} = 3.5$ h, $[M^{tot}]_0 = 35$ mM, $[S^{tot}]_0 = 35$ mM, and $[P{-}M_0^{tot}]_0 = 0.7$ mM. For the polymerization without the template, the same model parameters are used except for $k_b = k_a = k_f = k_d = 0$, $V^{tot}/V^b = 0$, $a = 0.9$, $t_{shift} = 5.0$ h, and $[S^{tot}]_0 = 0$. In both cases, the overall concentrations of the compounds, the polymerization rate k_p, the empirical constants a and t_{shift}, and the ratio between k_b and k_f follow from experiments, the values for ω_0 and E_a are based on literature values,[26] and the values of V^{tot}/V^b and k_{bn} are adjusted to fit the experimental data (cf. Supporting Information Section 10.2 for further details). (d) Comparison of the end structures formed by (1) performing the polymerization reaction without the template and subsequently mixing the resulting diblock with the template at 44 °C and (2) performing the polymerization reaction in the presence of the template at 44 °C.

of chemical feedback in these chemical networks are lacking. Yet, these insights are crucial; not only to optimize and rationally design synthetic reaction-assembly networks for nanomaterial fabrication, but also to provide a deeper understanding of how chemical feedback influences structure formation in vivo.

In this paper, we explore chemical feedback in a templated reaction-assembly network that couples covalent polymerizations to supramolecular electrostatic assembly on a macromolecular template. To unveil the kinetic pathways that underlie reaction progress, we perform time-resolved and in situ measurements based on high-resolution NMR spectroscopy and spectrally resolved relaxometry, complemented with light-scattering studies. While classical NMR spectroscopy has been used previously to study reaction-assembly networks,[13,16−18] we extend these NMR spectroscopy measurements with spectrally resolved NMR relaxation measurements to probe the local dynamics of the separate components, which is essential to unravel the underlying kinetic pathways of the network. Our experimental results reveal how the preassembly of monomers onto the oppositely charged template accelerates the covalent reaction and provides feedback to alter the supramolecular assembly process. On the basis of these experimental data, we establish a kinetic reaction-assembly model that quantitatively describes the underlying reaction pathways. These results can help both optimizing the design of synthetic reaction-assembly materials and resolving the role of chemical feedback in structure formation in vivo.

RESULTS AND DISCUSSION

Our templated reaction-assembly network consists of a neutral macromolecular chain-transfer agent P, positively charged monomers M as reagents and a negatively charged polyelectrolyte that forms the coassembly template, consisting of template binding sites S (Figure 1a). Specifically, we use poly(ethylene glycol methyl)ether 4-cyano-4-(propylsulfanylthiocarbonyl)-sulfanylpentanoate (PEG-CTA) as macromolecular chain-transfer agent, poly(sulfopropylmethacrylate) (PSPMA) with a degree of polymerization of 47 as the negative template, and vinylbenzyltrimethylammonium chloride (VBTAC) as the positive monomer. Reversible addition−fragmentation chain transfer (RAFT) polymerization of the positive monomer occurs at the end of the neutral chain, resulting in the growth of the diblock copolymer $P{-}M_n$. In the standard case, the targeted degree of polymerization of the positive block n is 50 and the ratio of monomer to template sites is 1:1. The reaction is performed at a potassium chloride (KCl) concentration of 35 mM. Both cationic monomer and the resulting cationic block of the diblock copolymer can bind to the template (Figure 1b), as evidenced by isothermal titration calorimetry measurements (Figure S1). When the cationic block grows sufficiently long, its binding to the anionic template induces micelle formation by complex coacervation. The complex of oppositely charged polyelectrolytes forms the micellar core, and the neutral block forms its corona. These charge-driven micelles are often referred to as complex coacervate core micelles (C3Ms).[25]

Phases in the Reaction-Assembly Process. To unravel the kinetic pathways that underlie this templated reaction-assembly network, we use a combination of NMR spectroscopy, spectrally resolved NMR relaxometry, and light scattering. We use NMR spectroscopy to monitor the monomer conversion and NMR relaxometry to probe the chemical details of the reaction-assembly network (Figure S2). The longitudinal relaxation time T_1 and transverse relaxation time T_2 both depend on the rotational correlation time τ_c of (part of) the molecule, with T_1 being mostly sensitive to fast molecular dynamics at the NMR measurement frequency and T_2 being mostly affected by static sources of restriction in the molecular

https://dx.doi.org/10.1021/acs.macromol.0c01915
Macromolecules 2020, 53, 10675−10685

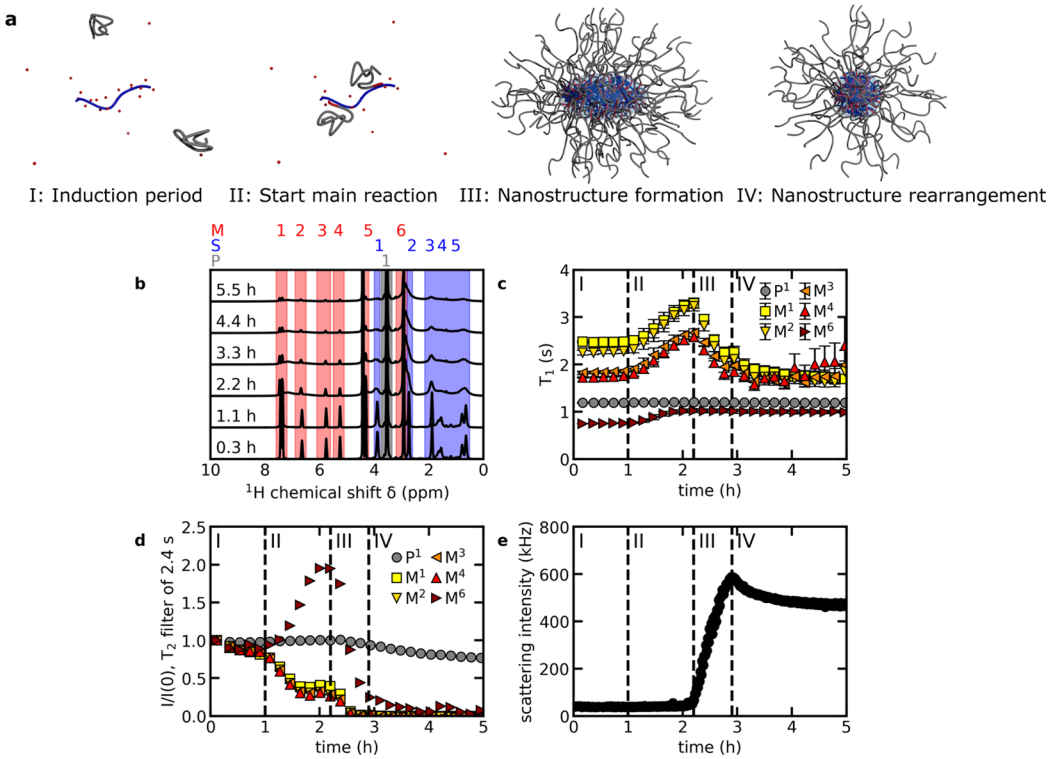

Figure 2. Different phases of the reaction-assembly process. (a) Schematic overview of the four different phases. At increasing reaction times of the templated reaction-assembly network, (b) ^{1}H NMR spectra; (c) T_1 values for the neutral block P and monomer M protons, with respective error bars obtained from single-exponential fitting; (d) T_2-filtered NMR spectral intensity (T_2-filter of 2.4 s) for the P and M protons, normalized to their own signal intensity at the start of the reaction; (e) light-scattering intensity.

reorientational dynamics.[27,28] Therefore, the combination of T_1 and T_2 measurements can be used to probe a wide range of mobility time scales, ranging from the fast dynamics of free monomers to the slow dynamics of polymers. The in situ determination of both T_1 and T_2 is complicated by the relatively large reaction speed compared to the time needed for quantitative T_1 and T_2 measurements. To obtain both sufficient time resolution and sufficient information on the local mobility of the components, we perform only quantitative T_1 measurements during the reaction while we take the changes in a T_2-filtered intensity as a measure for relative changes in T_2. We complement the ^{1}H NMR measurements with light-scattering measurements: while NMR relaxation measurements probe the local dynamics of the separate components, light-scattering measurements can probe the overall assembly of the different components together. Based on our experimental observations, we can distinguish four phases in the reaction-assembly process (Figure 2a), which are explained below.

Phase I: Induction Period. The reaction network is started by heating the reaction mixture, which leads to thermal decomposition of the radical initiator. First, we observe an induction period (Phase I) during which the monomer conversion is slow as revealed by monitoring the monomer conversion by ^{1}H NMR spectral measurements with a 0.02 s T_2 filter (Figure 1c).

Already at the start of this first phase, the situation with the template differs from the one without the template, in which there is no assembly and hence no chemical feedback. We observe that the longitudinal relaxation time T_1 of the monomer protons is shorter with the template than without the template (Table S1). For small molecules free in solution, both T_1 and T_2 decrease with increasing rotational correlation time of the molecule τ_c.[27,28] A decrease in T_1 in the presence of the template thus indicates restricted monomer mobility and can be explained by binding of monomers to the template. On the basis of T_1 measurements, we estimate that initially 50% of all monomers present binds to the oppositely charged template (Table S1). We note that differences among the T_1 values of the monomer protons are caused by differences in the intramolecular component of the dipole−dipole relaxation process. The latter process is driven by fluctuating fields generated via the interaction between two ^{1}H nuclear magnetic dipoles, and its intramolecular contribution is caused by nuclear vibrations and rotations within the molecule.[28]

The addition of the template substantially shortens the induction period (Figure 1c). We hypothesize that this is due to the local accumulation of monomers at the macromolecular template, leading to a local increase of monomer concentration. To verify that a higher (local) concentration can shorten the induction phase, we performed different polymerizations without the template at increasing monomer concentration, while keeping the concentration of chain-transfer agent and initiator the same (Figure 3a). Increasing the monomer concentration from 35 to 105 mM indeed shortens the induction period, while the final pseudo-first-order polymerization rate is the same in both cases (Figure 3b). Further increasing the monomer concentration to 175 mM only has a moderate effect on the induction phase. This reveals that the induction period consists of two contributions, one which is sensitive to the monomer concentration and another which is not. The contribution sensitive to monomer concentration can be explained by the fact that the first monomer added to a growing chain can have a lower effective reactivity as compared to subsequently added monomers, which has also been observed

https://dx.doi.org/10.1021/acs.macromol.0c01915
Macromolecules 2020, 53, 10675−10685

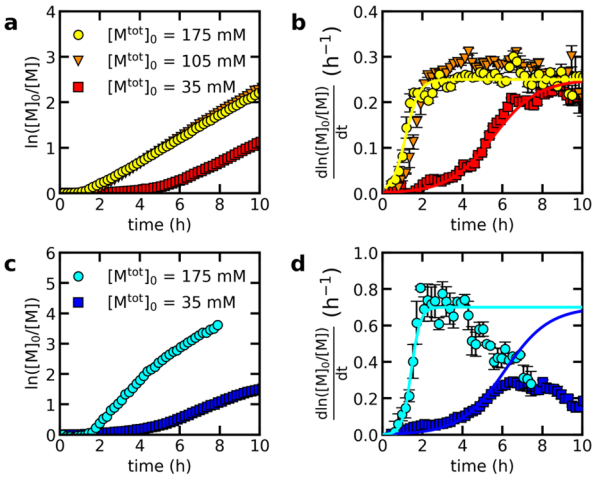

Figure 3. RAFT polymerizations without the template at different monomer concentrations. (a,b) Polymerization of the positive monomer (VBTAC) with the neutral block of Figure 1a as the chain-transfer agent. (a) Pseudo-first-order kinetic plot of the monomer conversion. (b) Local slope of the pseudo-first-order kinetic plot of (a) as a function of time. Error bars indicate uncertainty in the local slope determination. Solid lines are approximations of the experimental data based on the function $y = x(\exp(at - t_{shift}))/(1 + \exp(at - t_{shift}))$ with x = 0.25 and a = 0.9 and t_{shift} = 5.0 (35 mM) and a = 3.0 and t_{shift} = 3.5 (175 mM). (c,d) Polymerization of the negative monomer (KSPMA) with the neutral block of Figure 4a as chain-transfer agent. (c) Pseudo-first-order kinetic plot of the monomer conversion. (d) Local slope of the pseudo-first-order kinetic plot of (c) as a function of time. Error bars indicate uncertainty in the local slope determination. Solid lines are approximations of the experimental data based on the function $y = x(\exp(at - t_{shift})/(1 + \exp(at - t_{shift}))$; with x = 0.7 and a = 0.9 and t_{shift} = 5.5 (35 mM) and a = 4.5 and t_{shift} = 6.5 (175 mM).

in other RAFT polymerizations.[29] The contribution that is insensitive to monomer concentration is most likely due to a slow radical build-up at the reaction start, owing to the relatively low radical concentrations in our RAFT polymerization.

Phase II: Start Main Reaction. After the induction phase, the monomer conversion rate increases strongly, signaling the start of the main reaction (Phase II). For the polymerization with the template, the polymerization rate is strongly enhanced in this phase, as shown by the larger slope in the pseudo-first-order kinetic plot of the monomer conversion (Figure 1c). This is also due to the local increase of monomer concentration near the template due to binding and highlights the role of the template as a supramolecular staging area for the chemical reaction. We note that in another PIESA process the polymerization with the template was slower than without the template.[18] We hypothesize that this difference with our system is caused by the ∼17 times larger template concentration that was used in this other case, which will increase the viscosity and thus slow down the overall polymerization kinetics.

During Phase II, the T_1 of the monomer protons increases (Figure 2c), signaling an increase in the monomer mobility. The T_2-filtered ^{1}H NMR intensity decreases for all monomer protons except for M^6 (Figure 2d). This trend can be explained by noticing that an increase in the T_2-filtered signal intensity can be caused by an increase either in the monomer concentration and/or in T_2. Because the monomer concentration decreases in Phase II, the behavior of M^6 in Figure 2d is due to an increase in T_2, which confirms the increased monomer mobility as seen by T_1. For the other monomer protons, their T_2 also presumably increases in Phase II, but because their T_2 is longer than that of M^6, the underlying intensity increase that is induced by T_2 increase becomes negligible compared to the intensity decay because of monomer consumption (Supporting Information Section S3.2). These changes in T_1 and T_2 occur only for the polymerization with the template (Figure S3) and are thus the result of chemical feedback.

The onset of faster monomer reorientational dynamics in Phase II is the result of competitive template binding between the monomer and growing diblock copolymer, which binds with a higher affinity because of multivalency. The binding of the polymerizing positive blocks to the template is shown by the broadening of the template peaks in the ^{1}H NMR spectrum (Figure 2b). Broader peaks indicate a smaller T_2 and therefore a decrease in template mobility. The result of the competition between monomers and polymerizing blocks is that the concentration of template-bound monomer decreases, slowing down the polymerization rate at the template, as can be seen from the decrease in the slope of the monomer conversion during Phase II (Figure 1c).[18]

Phase III: Nanostructure Formation. In Phase III, coassembly of the templates with growing diblock copolymers leads to the nucleation of microphase-separated objects, as revealed by an increase in scattered light intensity (Figure 2e). Nanostructure formation in Phase III results in the net reduction of both T_1 and T_2 values of the monomer protons, except for M^6, suggesting that nanostructure formation somehow hinders the reorientational dynamics of the monomer (Figure 2c,d). Three possible causes, and combinations thereof, can be identified to explain the observed reduction in monomer mobility: (i) the incorporation of bound monomers within the nanostructures leads to a decrease in τ_c; (ii) an increase in the bound monomer fraction; (iii) an increase in the viscosity of the sample. The T_1 of the M^6 protons stays constant in Phase III, presumably because of that this chemical group is less affected by monomer incorporation in the nanostructure or viscosity increase or because increasing spectral overlap with the adjacent polymer peak prevents accurate evaluation of T_1 for the M^6 peak. Another possibility is that the τ_c of the M^6 protons is around $1/(\sqrt{2}\,\omega_L)$, where ω_L is the Larmor frequency. At this point, T_1 is less sensitive to changes in τ_c.[27,28]

Phase IV: Nanostructure Rearrangement. During Phase IV, continued polymerization and equilibration lead to a decrease in light-scattering intensity and apparent hydrodynamic radius (Figures 2e and S4). A possible explanation for this decrease is the transition from initially elongated objects into smaller spherical micelles. It is known that weakening of the electrostatic interactions can induce a change in shape from spheres to ellipsoids, for example, by the increase in ionic strength.[30] On the contrary here, as time progresses, the electrostatic interactions grow in strength as the length of the positive block increases, which could result in the transition from initially elongated objects into smaller spherical micelles. This rearrangement occurs only for shorter template lengths, while for longer templates the light-scattering intensity only increases during polymerization with a lower final intensity and smaller apparent hydrodynamic radius than for the shorter template lengths (Figure S5). This is in accord with literature results where the formation of ellipsoidal micelles was also observed only for shorter homopolymer lengths.[30] In fact, also for micelles formed at low concentration from the components of our system, transitions to larger nanostructures at ionic strengths above 10 mM happen only for the short template lengths (Figure S5).

https://dx.doi.org/10.1021/acs.macromol.0c01915
Macromolecules 2020, 53, 10675−10685

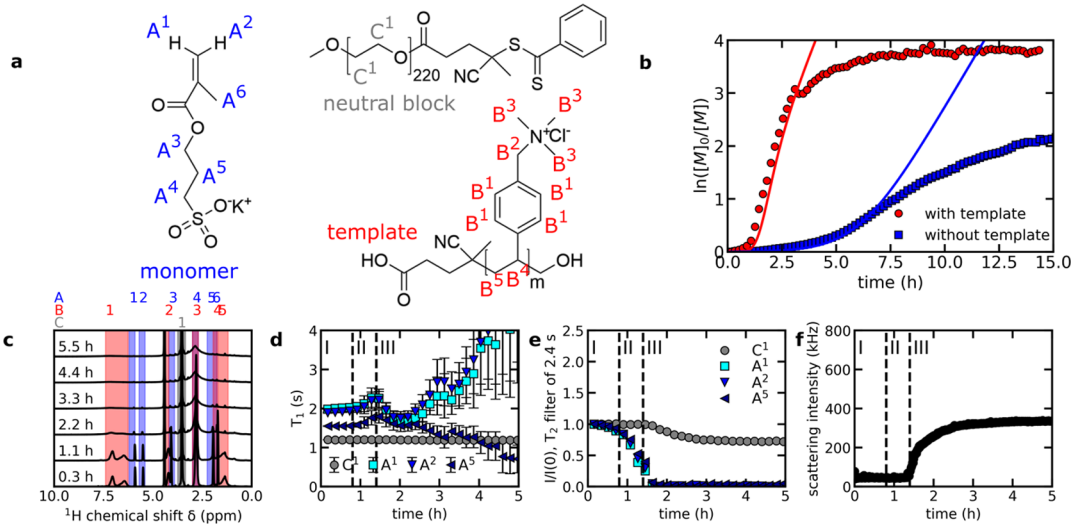

Figure 4. Inverted reaction-assembly network where a negatively charged block is polymerized in the presence of a positively charged template. (a) Different components of the inverted reaction-assembly network. (b) Pseudo-first-order kinetic plots of the monomer conversions for reactions with the template and without the template. Solid lines indicate model predictions for the polymerization with the template $k_p = 1.0\ \mathrm{mM^{-1}\ h^{-1}}$, $k_b = k_a = 12\ \mathrm{mM^{-1}\ h^{-1}}$, $k_{bn} = 500k_b$, $k_d(n) = \omega_0 \exp(-nE_a/k_BT)$ with $\omega_0 = 3.1 \times 10^4\ \mathrm{h^{-1}}$ and $E_a = 6k_BT$, $k_f = k_d(1)$, $V^{tot}/V^b = 8$, $a = 4.5$ and $t_{shift} = 6.5$ h, $[M^{tot}]_0 = 35$ mM, $[S^{tot}]_0 = 35$ mM, and $[P{-}M_0^{tot}]_0 = 0.7$ mM. For the polymerization without the template, the same model parameters are used except for $k_b = k_a = k_f = k_d = 0$, $V^{tot}/V^b = 0$, $a = 0.9$, $t_{shift} = 5.5$ h, and $[S^{tot}]_0 = 0$. At increasing reaction times of the templated reaction-assembly network, (c) ^{1}H NMR spectra; (d) T_1-values for neutral block C and the monomer A protons, with respective error bars obtained from single-exponential fitting; (e) T_2-filtered NMR spectral intensity (T_2-filter of 2.4 s) for the C and A protons, normalized to their own signal intensity at the start of the reaction; (f) light-scattering intensity.

Future time-resolved small-angle X-ray scatting (SAXS) measurements could help to verify whether the decrease in light scattering is indeed caused by rearrangements into smaller structures. At the moment, we cannot exclude that other factors than the nanostructure size have affected the light-scattering intensity because the concentration of the reaction-assembly network is relatively high for light-scattering experiments, and therefore multiple-scattering events or interactions between the different scattering objects might occur, which can affect the light-scattering intensity and the apparent hydrodynamic radius.

The nanostructure formation and rearrangement can also be observed from the decrease in T_2 of the neutral block (Figure 2d). This decrease in T_2 agrees well with the proposed micelle formation: when the neutral block becomes integrated into a dense micellar corona, its mobility is restricted, resulting in a lower T_2. The neutral block in the final equilibrium nanostructures exhibits three distinct T_2 values, while at the start of the reaction it has a single T_2 (Figure S6). The three distinct T_2 values reveal the occurrence of three main local mobility environments for protons that might be assigned to, in order of increasing local mobility, protons close to micelle core, protons in the middle of the micelle corona, and protons in the outer part of the micelle corona. This might also explain why the T_2-filtered signal decreases during Phase IV: the part of the corona close to the core becomes denser when the micelles become spherical. This means that locally the mobility of the protons close to the core gets lower, and thus, the overall average T_2 decreases even though protons further away from the core can have an increase in mobility upon transition to spherical micelles and their T_2 might slightly increase. While, as expected, T_2 is sensitive to slow reorientational dynamic modes, we find that the T_1 of the neutral block is not much affected by the nanostructure formation (Figure 2c). It might be that the τ_c of the neutral block is around $1/(\sqrt{2}\,\omega_L)$, where T_1 is less sensitive to changes in τ_c.[27,28] Similar behavior of T_1 and T_2 of the neutral block upon C3M formation have been measured earlier at equilibrium conditions.[31]

The occurrence of these four different phases is not restricted to this particular reaction-assembly network: also for a shorter and longer template length, we observe the same phases (Figure S5), with the nanostructure reorganization phase being absent for the longest template length, as discussed above. This demonstrates the relative robustness of our observations. We note that variations between repetitions of the same reaction-assembly experiment (Figures S5 and S7) could be explained by small differences in the trace amount of oxygen present, which results in slightly different radical concentrations. These variations do not affect the general trends: in all these measurements, the polymerization rate in the presence of the template is faster than that in the absence of the template, and at certain point in the reaction, the polymerization rate decreases.

Inverted System. To further verify the robustness of our description of these templated reaction-assembly networks, we invert the system by polymerizing a negatively charged block in the presence of a positively charged template (Figure 4a). In this way, we change both the monomer−monomer interactions at the template (Figure S1) and the polymerization reactivity (Figure 3c,d). The inverted system also shows a feedback-enhanced reaction rate as compared to the polymerization without the template (Figure 4b). In addition, T_1 measurements show that also for the inverted system about 50% of all monomers initially binds to the oppositely charged template (Table S2). Furthermore, the inverted system undergoes the same reaction-assembly network phases: initially the monomer conversion is also slow (Figure 4b). Subsequently, when the main reaction starts, the template peaks also broaden (Figure 4c) and the monomer T_1 increases (Figure 4d). The monomer T_1 decreases again when the nanostructure formation starts and also the T_2 of the neutral block decreases upon nanostructure formation (Figure 4e). The inverted system does not show

https://dx.doi.org/10.1021/acs.macromol.0c01915
Macromolecules 2020, 53, 10675−10685

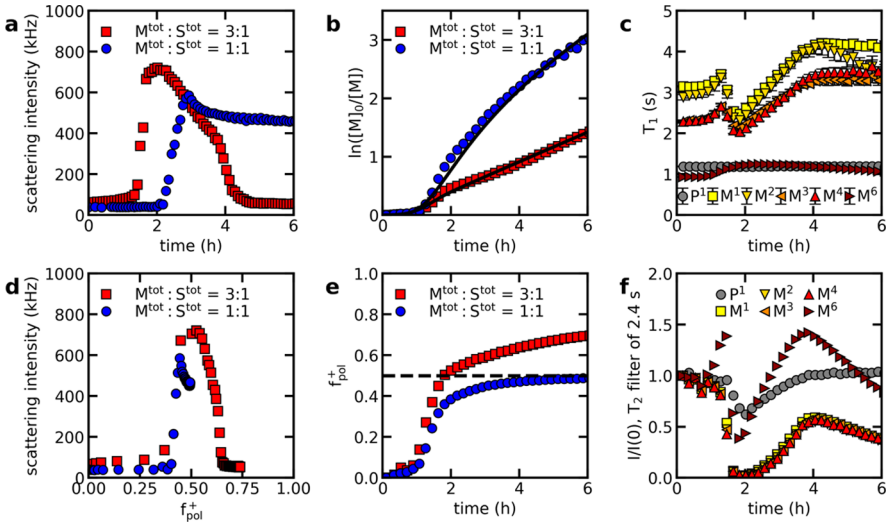

Figure 5. Effect of the monomer-to-template ratio M^{tot}/S^{tot}. (a) Light-scattering intensity during the reaction-assembly process. (b) Pseudo-first-order kinetic plot of the reaction-assembly process. Solid lines indicate model predictions with the same model parameters as in Figure 1, except for the initial monomer concentration for M^{tot}/S^{tot} = 3:1, which is $[M^{tot}]_0$ = 105 mM. (c) T_1-values of P and M protons during the reaction-assembly process for M^{tot}/S^{tot} = 3:1 with respective error bars obtained from single-exponential fitting. (d) Light-scattering intensity as a function of fractional polymer charge ratio f_{pol}^+. (e) Positive polymer fraction f_{pol}^+ during the reaction-assembly process. The dashed line indicates the point of equal charge stoichiometry of the oppositely charged polyelectrolytes. (f) Changes in the T_2-filtered NMR spectral intensity (T_2-filter of 2.4 s) for the P and M protons, normalized to their own signal intensity at the start of the reaction, for the M^{tot}/S^{tot} = 3:1 reaction-assembly process.

nanostructure rearrangement: the scattered light intensity only increases during the polymerization reaction (Figure 4f), similar to the reaction-assembly network with the longest negatively charged template. This is because the positively charged template is probably longer than the negatively charged template that we used for Figure 2.

Effect of Reactant Stoichiometry. So far, we have focused on reaction networks with a 1:1 ratio of monomer-to-template sites. The reaction-assembly process and the underlying kinetics can be tuned by various parameters, such as the reactant stoichiometry. If we add an excess of monomer compared to the number of template sites at a 3:1 ratio, first nanostructures form and then disassemble again (Figure 5a). This is similar to what has been observed for another PIESA reaction[16] and agrees with the observations that C3Ms can be formed only around equal charge stoichiometry.[25,32]

Changing the reactant stoichiometry affects the relative polymerization rate and the evolution of T_1 and T_2 of the monomers and neutral block during the reaction. The relative polymerization rate is slower when we add an excess of monomer (Figure 5b) because a smaller fraction of the total monomer can preassemble at the template, as it becomes saturated. This is reflected by the larger monomer T_1 values at the start of the reaction (Figure 5c). The increase in T_1 at the start of the main reaction again indicates expulsion of the monomer from the template because of binding competition and the subsequent T_1 decrease again coincides with the start of the nanostructure formation, which reduces the monomer mobility. As the reaction time progresses, the point of equal charge stoichiometry is crossed, leading to an excess of positive block units as compared to template sites. This results in the disintegration of the nanostructures into soluble complexes, where the excess part of the positive block is free in solution and the other part of the positive block is bound to the template, as evidenced by ^{1}H NMR spectroscopy (Figure S8). The nanostructure disassembly results in an increase of the T_1 of the monomer protons. After 4 h, when the nanostructures are completely disassembled (Figure 5a), the T_1-values of the monomers in the reaction network values have approached the T_1 values of free monomers in the absence of a template (Table S1). After this point, the T_1 values of the monomers remain constant. The apparent decrease of T_1 of the M^2 proton peak is probably because of partial overlap with the NMR signal of the adjacent peak of positive polymer formed during the reaction. The measured T_1 of the M^6 proton peak is not much affected by the nanostructure formation, as was also observed in the 1:1 ratio case. The T_2-filtered intensity of the monomers shows similar trends as T_1 (Figure 5f), except in that it decreases after 4 h, most probably because of the concurrent effects due to variations in monomer concentration and in T_2: after 4 h, the amount of monomer keeps decreasing, thus lowering the T_2-filtered intensity, while T_2 probably remains constant. The decrease and subsequent increase in T_2-filtered intensity of the neutral block reflect the nanostructure formation and subsequent disassembly.

The change in stoichiometry not only affects the reaction rate and the final structure formed but also the (intermediate) structures that are formed at equal charge stoichiometry of both polyelectrolytes. The polyelectrolyte charge stoichiometry can be expressed by the fractional polymer charge ratio $f_{pol}^+ = [pos]/([pos] + [neg])$, where [pos] and [neg] are the concentrations of monomers that are part of a polycation and polyanion, respectively. At equal charge stoichiometry, $f_{pol}^+ = 0.5$. In excess of monomer, the intermediate structures at $f_{pol}^+ = 0.5$ scatter more light, indicating that different structures are formed. This difference can be explained from the effect of stoichiometry on the absolute reaction rate: although the relative reaction rate is lower when the monomer is present in excess, the absolute reaction rate is still higher. This can be seen by comparing the increase of the degree of polymerization of the positive block (Figure 5e). Especially around $f_{pol}^+ = 0.5$, the polymerization with excess monomer is faster. This higher absolute rate is the result of the larger overall monomer concentration.

https://dx.doi.org/10.1021/acs.macromol.0c01915
Macromolecules 2020, 53, 10675−10685

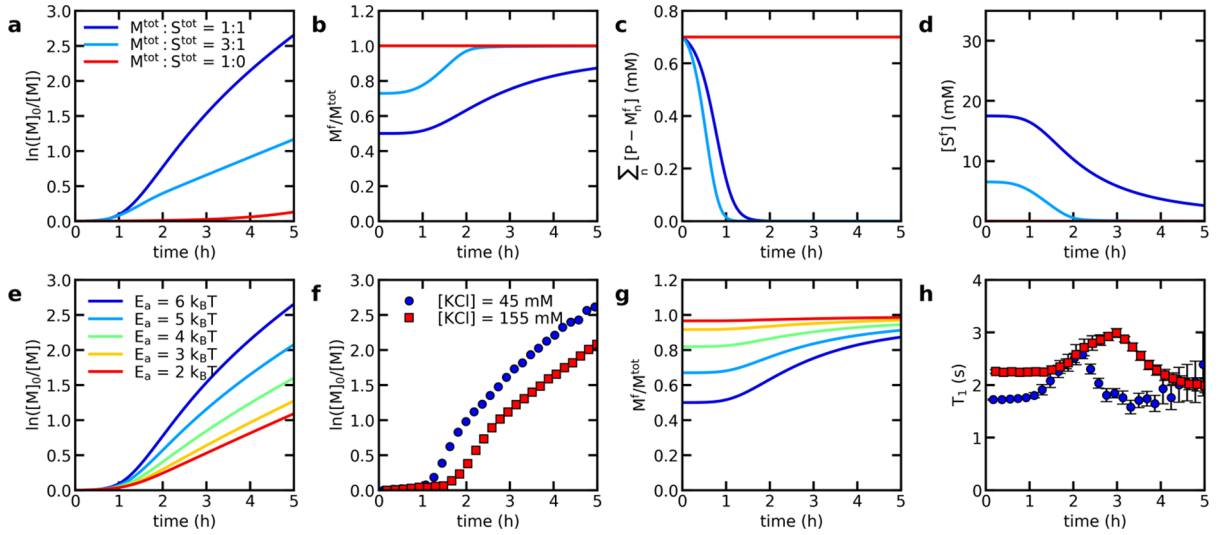

Figure 6. Kinetic model predictions and the effect of the monomer−template interaction strength. (a−e,g) Kinetic model predictions for (a,e) the time evolution of the monomer concentration, (b,g) free monomer fraction M^f/M^{tot}, (c) free diblock copolymer concentration $\sum_n[P-M_n^f]$, and (d) free template sites concentration. Model predictions are made for the polymerization reaction with different monomer-to-template ratios (a−d) and for the polymerization reaction with template at M^{tot}/S^{tot} = 1:1 with decreasing monomer binding strengths by decreasing the value of E_a (e,g), which affects both k_d and k_f. Unless otherwise indicated, the model parameters are the same as in Figure 1. (f,h) Experimental effects of decreasing the monomer binding strength by increasing the ionic strength (KCl concentration) in the reaction-assembly network on (f) the monomer conversion and on (h) the T_1 of the monomer proton M[4].

This reveals the important role that the kinetic pathways play in structure formation: the building blocks form different structures when the rate at which they approach the point of equal charge stoichiometry is higher. This is seen by the fact that the scattering intensity is higher when the rate of polymerization around f_{pol}^+ = 0.5 is increased. Moreover, direct mixing of presynthesized polymers at f_{pol}^+ = 0.5, where equal stoichiometry is achieved almost instantly, results in very turbid samples (Figure 1d). This suggests that in this case kinetically trapped structures are formed when building block synthesis and assembly are decoupled. Indeed, during C3M formation larger nonequilibrium clusters are sometimes observed to be formed, which can either relax to their equilibrium state[33,34] or remain trapped if equilibration is too slow.[33,35] Gradual transition across the energy landscape for coassembly by coupling synthesis with assembly can avoid the formation of these trapped structures, without necessitating laborious protocols in which salt is gradually removed to slowly increase the interaction strength.[36]

Kinetic Model. These data shed light on the fundamental effects that chemical feedback can have on the templated coassembly process explored here. To obtain a quantitative grasp on these effects for a predictive understanding of reaction-assembly networks, we develop a kinetic reaction network model that captures the elementary reaction steps and their couplings. Polymerization can take place both at the template and in solution, with a rate constant k_p. At the template, the monomer concentration is locally increased because of supramolecular binding. The factor by which the concentration is increased depends on the ratio of the volume around the template compared to the total volume V^b/V^{tot} and the monomer fraction that is bound to the template. This fraction depends on the number of available free binding sites S^f and on the monomer binding affinity. The binding affinity is reflected in the ratio between the binding constant k_b and release constant k_f of the monomer to the template. The positive block binds stronger to the template because of multivalency: $k_d = \omega_0 \exp(-nE_a/k_BT)$, where E_a is the binding energy of a single monomer unit to the template. The diblock binds to the template with an association rate k_a, which is diffusion-limited. The positive monomers of a bound diblock can temporarily release from the template and subsequently bind again. As long as part of the monomers of the bound diblock remain bound, this temporal release of some of the monomers will not result in the release of the diblock from the template. The release rate constant of a diblock monomer is the same as the dissociation constant for a single monomer k_f. However, we expect that the binding rate constant k_{bn} is larger than the binding constant of a single monomer k_b because the free monomers of the bound diblock remain close to the template. The different processes of the kinetic reaction network model are schematically summarized in Figure 1b. For visual clarity, the reaction of the free diblock with the bound monomers, the reaction of the bound diblock with the free monomers, and the exchange of the bound monomers of the bound diblock between a template-bound and a free state are not shown in Figure 1b.

The polymerization rate in our kinetic model has to be corrected to account for the experimentally observed induction period. For this, we use the polymerizations without the template at different monomer concentrations to obtain experimentally derived correction functions $c(t)$ (Figure 3). For the polymerization with the template, we obtain the $c(t)$ from the polymerization without the template at a monomer concentration of 175 mM. This is an approximation because the local monomer concentration at the template is not exactly 175 mM, and the monomer concentration is only locally increased. However, at larger monomer concentrations, the effect of the monomer concentration on the induction period is small compared to monomer independent induction time. Therefore, we expect that these differences only have a minor effect and the approximation will work reasonably well. The correction functions $c(t)$ follow from the local slopes of the pseudo-first-order kinetic plots: for pseudo-first-order polymerization kinetics, this slope equals $k_p\sum_n[P-M_n]$, where k_p is the polymerization rate constant per molar of polymer $\sum_n[P-$

https://dx.doi.org/10.1021/acs.macromol.0c01915
Macromolecules 2020, 53, 10675−10685

M_n]. The factor by which the local slope at time t deviates from this value gives the correction value $c(t)$. We note that for the polymerization of the inverted system, deviations from pseudo-first-order kinetics do not happen only at the start of the reaction but also at the end probably because of radical termination reactions (Figure 3c,d). Because we expect the termination reactions to be slightly different for every polymerization reaction, we do not include these effects in $c(t)$. In order to numerically solve the differential equations of the kinetic model, we need a better time resolution than we can obtain from the NMR reaction experiments. Therefore, we approximate the local slope function by the function $y = x(\exp(at - t_{shift}))/(1 + \exp(at - t_{shift})) = xc(t)$, where x should equal $x = k_p\sum_n[P{-}M_n]$ and a and t_{shift} are empirical constants (Figure 3b,d).

The covalent and supramolecular reactions together can be described by a set of differential reaction kinetic equations (Methods). Once the initial concentrations and model constants are known, this system of differential equations can be numerically solved to give the concentrations of the different components as a function of the reaction time. Most rate constants are obtained from additional experiments or the literature;[26] see Supporting Information Section S10 and Figures S10−S17 for parameterization details. We use only the ratio V^{tot}/V^b and the binding rate of the unbound monomers of the bound diblock k_{bn} as adjustable parameters to fit the model to the experimental data. By taking $V^{tot}/V^b = 8$ and $k_{bn} = 500k_b$, the model prediction of the monomer conversion agrees well with the experimental data for the reaction-assembly network with the negatively charged template (Figures 1c and 5b). In addition, it also correctly describes the time point of free monomer fraction increase (Figures 6b, 2c,d, 5c,f). For the inverted reaction-assembly network, the model overestimates the reaction rate at longer reaction times (Figure 4b) because we did not include the effect of radical termination in the model $c(t)$ function as explained above. The obtained value for V^{tot}/V^b is smaller than that we estimated based on estimations of the ionic bond length and polyelectrolyte blob size (Figure S9). Possible explanations for this difference are that the bound monomers might also be further away than the ionic bond length or that neglecting the prefactors in the estimation resulted in an overestimation of the V^{tot}/V^b ratio. In addition, viscosity effects might have slightly slowed down the polymerization, resulting in a lower apparent V^{tot}/V^b ratio in the experiments. The fact that k_{bn} has to be much larger than the binding rate constant of a single monomer k_b to accurately describe the data (Figure S11) demonstrates once more that local enrichment can significantly increase the rate at which the process occurs.

The free diblock copolymer concentration decreases before we observe the increase in the fraction of free monomers (Figure 6c). Only when the average degree of polymerization increases sufficiently such that the binding affinity of the diblock becomes larger, the bound monomer fraction decreases. The increased binding affinity of the diblock results in a decrease in free template sites S^f (Figure 6d). This decrease in S^f shifts the monomer-to-template binding equilibrium more toward the free monomers. The binding of the diblock to the template is reflected by the broadening of the template proton peaks in the ^{1}H NMR spectra (Figures 2b, S8).

Within our model, the template plays an essential role by acting as staging area for the chemical reaction. By decreasing the monomer−template interactions, the template effect can be reduced: decreasing the binding energy E_a of a monomer to the template results in less monomer binding and as a result the reaction rate is decreased (Figure 6e,g). In fact, for the lowest binding energies, the decrease might even be larger than shown here because the induction period and thus $c(t)$ are also affected when the monomer concentration largely decreases (Figures 3 and S12). A way to decrease the interaction strength experimentally is to increase the ionic strength in the solution. A higher ionic strength indeed lowers the monomer binding and the reaction rate (Figures 6f,h and S18). In addition, the induction period seems to lengthen at higher ionic strength, which could indicate that the decrease in local monomer concentration is large enough to affect the induction period. These effects of changing the interaction strength demonstrate that the reaction rate of the templated reaction-assembly network can be tuned, which is essential to regulate the assembly and in some cases can regulate the final structures formed, as discussed above.

CONCLUSIONS

The rational design of synthetic reaction-assembly strategies requires a deep understanding of the chemical feedback between the covalent reaction and the supramolecular assembly. Here, we have unraveled the kinetic pathways of templated reaction-assembly networks and we have shown that chemical feedback fundamentally changes both processes. Supramolecular staging of the monomers on the template strongly accelerates the polymerization reaction. The rate at which the reaction reaches the point of self-assembly in turn affects the structures that are formed.

One of the challenges in the design of self- or coassembling systems is to ensure that they arrive at their equilibrium state and do not become trapped in a local energetic minimum. Our results highlight how the rational design of a reaction-assembly network can achieve exactly this also at relatively high concentrations, where kinetic trapping is often inevitable in conventional assembly processes.[37] These results can be easily extended to other PIESA and PISA systems, where kinetic trapping is avoided or in some cases promoted to arrive at new nanostructures.[14,16,17] Also, in these other reaction-assembly networks, spectrally resolved NMR relaxometry can be applied to probe the local dynamics of the separate components. Simultaneously, our kinetic model can serve as a framework to describe also these other systems after implementing some adaptations, for example, including viscosity effects or replacing local enrichment at the template by local enrichment within assembled structures. It would be interesting to complement these future measurements by time-resolved SAXS measurements as the interpretation of SAXS measurements at the relatively high concentrations of the reaction-assembly networks is less ambiguous than for conventional light-scattering experiments. By using this combination of NMR experiments, scattering experiments, and kinetic modeling, the assembly of a wide variety of nanostructures can be linked to the corresponding reaction kinetics, facilitating the rational design of new synthetic supramolecular materials.

METHODS

Sample Preparation. A comprehensive overview of synthetic methods is provided in the Supporting Information (Section S1). For the reaction-assembly experiment at M^{tot}/S^{tot} = 1:1, the positive monomer vinylbenzyltrimethylammonium chloride (VBTAC, 35 mM), the macroRAFT chain-transfer agent poly(ethylene glycol methyl)ether 4-cyano-4-(propylsulfanylthiocarbonyl)-sulfanylpentanoate (PEG-CTA, 0.7 mM), the radical initiator 2,2′-azobis[2-(2-

https://dx.doi.org/10.1021/acs.macromol.0c01915
Macromolecules 2020, 53, 10675−10685

imidazolin-2-yl)propane] dihydrochloride (VA-044, 0.14 mM), the template poly(sulfopropylmethacrylate) (PSPMA, 35 mM of SPMA units), and potassium chloride (KCl) (10 mM) were dissolved in 5 mL of D_2O. The solution was degassed with N_2 for 30 min. Simultaneously, a glass tube for light-scattering experiments and a NMR tube both sealed with a rubber septum were also degassed for 30 min. Subsequently, circa ∼0.8 mL was transferred to the NMR tube and ∼3.5 mL was transferred to the glass tube.

For the polymerization at a M^{tot}/S^{tot} = 3:1 ratio, the monomer concentration was 105 mM instead of 35 mM, for the polymerizations without the template, no PSPMA was added, and for the polymerization at larger ionic strength, 120 mM KCl was added instead of 10 mM.

The sample preparation protocol for the inverted reaction-assembly network was similar to the sample preparation protocol for the normal reaction-assembly network with [VBTAC] = 35 mM. Only this time, the negatively charged PSPMA template was replaced by the positively charged poly((vinylbenzyl)trimethylammoniumchloride) (PVBTA) template and the positively charged VBTAC monomer was replaced by the negatively charged 3-sulfoproyl methacrylate potassium (KSPMA) monomer. In addition, the PEG chain-transfer agent was replaced by another PEG chain-transfer agent, poly(ethylene glycol)4-cyano-4-phenylcarbonothioylthio pentanoate. For the polymerizations without the template, no PVBTA was added.

Light-Scattering Measurements. Light-scattering measurements were performed at 44 °C on ALV light-scattering apparatus equipped with an ALV/LSE-5004 light scattering electronic and multiple tau digital correlator and a HeNe-laser operating at 632.8 nm. The scattering angle was set at 90°. The scattered intensities were obtained by averaging the photon count rate over periods of 60 s. The apparent hydrodynamic radius was obtained from second-order cumulant analysis of the intensity autocorrelation function (Figure S4).

NMR Measurements. ^{1}H NMR reaction experiments were performed at 44 °C on a Bruker 700 MHz AVANCE NMR equipped with a BBI probe. During the reaction, a set of four different NMR measurements was continuously repeated, consisting of (i) single-pulse spectral acquisition; (ii) single-pulse spectral acquisition with a T_2-filter based on PROJECT pulse sequence[38] (short filter of 20 ms, Section S3.1 and Figure S2); (iii) same as in (ii) but with long T_2-filter of 2.4 s (Section S3.2); (iv) inversion recovery measurement with a PROJECT-based acquisition scheme (Section S3.3 and Figure S2). Here, measurements (ii), (iii), and (iv) were used, respectively, to quantify the monomer conversion, to observe indirect effects of T_2 on signal intensity, and to determine T_1 relaxation rates. The length of the 90° rf pulse was readjusted at the start of every reaction and was subsequently kept constant within the reaction study. A 14 kHz spectral width was used. In each experiment, the signal from two consecutive acquisitions was added to obtain a sufficient signal-to-noise ratio. The receiver dead time was set to 6.5 μs. The longest T_1 was about 3−4 s during most of the reaction, thus the recycle delay was set to 21 s ($\sim 5T_1$) to obtain quantitative results while achieving the desired time resolution. Only at the end of the reactions with template at M^{tot}/S^{tot} = 3:1 and during the reactions without template, the T_1 of one M peaks (M^2) exceeded 4.2 s (Figure S2); thus, this particular result is not fully quantitative. Yet, this does not affect the data interpretation presented here. The M^5 proton peak partly overlaps with the solvent peak and the A^3, A^4, and A^6 proton peaks (partly) overlap with the template proton peaks. Therefore, these protons are not included in the analysis of T_1 and of the T_2-filtered intensity. After the reaction, the measured free induction decays were Fourier transformed, phased, baseline corrected, and integrated by using the Bruker NMR software TopSpin 4.0.7. Single-exponential data fitting of T_1 recovery curves was performed by using a constrained nonlinear least-squares fit algorithm as implemented in the Python package SciPy.

Kinetic Model. The kinetic model describes the changes in the concentration of the different components with a set of differential equations. Here, we give a brief overview of these equations. More details are given in the Supporting Information (Section S10).

The change in free monomer concentration is given by

$$\frac{d[M^f]}{dt} = -k_b[M^f][S^f] + k_f[M^b] - k_p c(t)[M^f]\left(\sum_n [P - M_n^f] + \sum_n [P - M_n^b]\right) \quad (1)$$

where the first two terms indicate the change of free monomer concentration because of the exchange of the monomer between the free and the bound state and the last term indicates the change due to the polymerization reaction. In a similar way we get for the bound monomer

$$\frac{d[M^b]}{dt} = k_b[M^f][S^f] - k_f[M^b] - k_p c(t)[M^b]\left(\frac{V^{tot}}{V^b}\sum_n [P - M_n^b] + \sum_n [P - M_n^f]\right) \quad (2)$$

here, the factor V^{tot}/V^b accounts for the fact that the monomer concentration at the template is locally increased.

The change in concentration of a free diblock with a degree of polymerization of the positive block n is given by

$$\frac{d[P - M_n^f]}{dt} = -k_a[S^f][P - M_n^f] + k_d(n)[P - M_n^b] + k_p c(t)([M^f] + [M^b])([P - M_{n-1}^f] - [P - M_n^f]) \quad (3)$$

also here, the first two terms correspond to exchange between the free and the bound state and the last term corresponds to the polymerization reaction.

The change in the concentration of a bound diblock with the degree of polymerization of the positive block n follows from

$$\frac{d[P - M_n^b]}{dt} = k_a[S^f][P - M_n^f] - k_d(n)[P - M_n^b] + k_p c(t)\left([M^f] + \frac{V^{tot}}{V^b}[M^b]\right)([P - M_{n-1}^b] - [P - M_n^b]) \quad (4)$$

The neutral block P−M_0 cannot bind to the template and therefore always remains in the free state. Its concentration decreases due to the polymerization reaction

$$\frac{d[P - M_0^f]}{dt} = -k_p c(t)([M^f] + [M^b])[P - M_0^f] \quad (5)$$

When a diblock with n positive monomers is bound to the template, part of the monomers can also temporarily unbind from the template and rebind again. The positive monomers of bound diblocks can thus exchange between a free and a bound state. We indicate the concentration of bound positive monomers of bound diblocks with $[n^b]$ and the concentration of free positive monomers of bound diblocks with $[n^f]$. The concentration of bound positive monomers of bound diblocks $[n^b]$ changes according to

$$\frac{d[n^b]}{dt} = k_{bn}[n^f][S^f] - k_d(1)[n^b] + k_a[S^f]\sum_n [P - M_n^f]n - z\sum_n k_d(n)[P - M_n^b]n + k_p c(t)\left([M^f] + \frac{V^{tot}}{V^b}[M^b]\right)\sum_n [P - M_n^b] \quad (6)$$

where $z = [n^b]/([n^b] + [n^f])$ is the fraction of bound monomers of the positive block. The first two terms correspond to the exchange between the free and bound state. The third and fourth terms indicate the

https://dx.doi.org/10.1021/acs.macromol.0c01915
Macromolecules 2020, 53, 10675−10685

changes in $[n^b]$ because of binding and release of the diblock, respectively, and the last term indicates the increase in $[n^b]$ when a bound diblock reacts with a free monomer.

The change in the concentration of free positive monomers of bound diblocks $[n^f]$ is given by

$$\frac{d[n^f]}{dt} = -k_{bn}[n^f][S^f] + k_d(1)[n^b] - (1-z)\sum_n k_d(n)[P-M_n^b]n \quad (7)$$

Finally, the change of the free template site concentration is given by

$$\frac{d[S^f]}{dt} = -k_b[M^f][S^f] + k_f[M^b] - k_a[S^f]\sum_n [P-M_n^f]n + z\sum_n k_d(n)[P-M_n^b]n - k_{bn}[n^f][S^f] + k_d(1)[n^b] + k_p c(t)\left([M^b]\sum_n [P-M_n^f] - [M^f]\sum_n [P-M_n^b]\right) \quad (8)$$

where the first two terms correspond to the binding and release of a single monomer, the third and fourth terms correspond to the binding and release of a diblock, the fifth and sixth terms correspond to the binding and release of the monomers of the bound diblocks, and the last term accounts for changes in $[S^f]$ because of the reactions of a bound monomer with a free diblock or a free monomer with a bound diblock.

We have used the Runge−Kutta fourth-order method to numerically solve this system of differential equations for different sets of model parameters (Figures S10−S17).

■ ASSOCIATED CONTENT

Supporting Information

The Supporting Information is available free of charge at https://pubs.acs.org/doi/10.1021/acs.macromol.0c01915.

Polymer synthesis; isothermal titration calorimetry measurements; overview of the ^{1}H NMR measurement methods used to monitor the reaction-assembly network; estimation of the initial bound monomer fraction from NMR T_1 measurements; polymerization without template; apparent hydrodynamic radius from light-scattering measurements; effect of the template length; ^{1}H NMR T_2 measurements of the neutral block; reactant stoichiometry effects; and kinetic model details and the reaction-assembly network at 155 mM KCl (PDF)

■ AUTHOR INFORMATION

Corresponding Author

Joris Sprakel − *Physical Chemistry and Soft Matter, Wageningen University & Research, 6708 WE Wageningen, The Netherlands;* orcid.org/0000-0001-6532-4514; Email: joris.sprakel@wur.nl

Authors

Inge Bos − *Physical Chemistry and Soft Matter, Wageningen University & Research, 6708 WE Wageningen, The Netherlands;* orcid.org/0000-0003-1097-3650

Camilla Terenzi − *Laboratory of Biophysics, Wageningen University & Research, 6708 WE Wageningen, The Netherlands;* orcid.org/0000-0003-3278-026X

Complete contact information is available at: https://pubs.acs.org/10.1021/acs.macromol.0c01915

Author Contributions

I.B. and J.S. conceived and designed the project. I.B. synthesized and characterized all compounds. I.B. and C.T. performed experimental work and analysis. I.B. performed the modelling. All authors cowrote the manuscript.

Notes

The authors declare no competing financial interest.

■ ACKNOWLEDGMENTS

This research was supported by the Netherlands Organization for Scientific Research (NWO) through the VIDI (project number 723.016.001) research programme. C.T. acknowledges funding from the 4TU Precision Medicine program supported by High Tech for a Sustainable Future.

■ REFERENCES

(1) Govindarajan, S.; Nevo-Dinur, K.; Amster-Choder, O. Compartmentalization and spatiotemporal organization of macromolecules in bacteria. *FEMS Microbiol. Rev.* **2012**, *36*, 1005−1022.

(2) Zhou, H.-X.; Rivas, G.; Minton, A. P. Macromolecular crowding and confinement: biochemical, biophysical, and potential physiological consequences. *Annu. Rev. Biophys.* **2008**, *37*, 375−397.

(3) Dykeman, E. C.; Stockley, P. G.; Twarock, R. Solving a Levinthal's paradox for virus assembly identifies a unique antiviral strategy. *Proc. Natl. Acad. Sci. U.S.A.* **2014**, *111*, 5361−5366.

(4) Zhang, G.; Hubalewska, M.; Ignatova, Z. Transient ribosomal attenuation coordinates protein synthesis and co-translational folding. *Nat. Struct. Mol. Biol.* **2009**, *16*, 274.

(5) Zhdanov, V. P. Viral capsids: Kinetics of assembly under transient conditions and kinetics of disassembly. *Phys. Rev. E: Stat., Nonlinear, Soft Matter Phys.* **2014**, *90*, 042721.

(6) Verdier, T.; Foret, L.; Castelnovo, M. Modeling the kinetics of open self-assembly. *J. Phys. Chem. B* **2016**, *120*, 6411−6420.

(7) Komar, A. A. A pause for thought along the co-translational folding pathway. *Trends Biochem. Sci.* **2009**, *34*, 16−24.

(8) Whitesides, G. M.; Grzybowski, B. Self-assembly at all scales. *Science* **2002**, *295*, 2418−2421.

(9) Lehn, J.-M. From supramolecular chemistry towards constitutional dynamic chemistry and adaptive chemistry. *Chem. Soc. Rev.* **2007**, *36*, 151−160.

(10) Yan, X.; Wang, F.; Zheng, B.; Huang, F. Stimuli-responsive supramolecular polymeric materials. *Chem. Soc. Rev.* **2012**, *41*, 6042−6065.

(11) Chakrabarty, R.; Mukherjee, P. S.; Stang, P. J. Supramolecular coordination: self-assembly of finite two-and three-dimensional ensembles. *Chem. Rev.* **2011**, *111*, 6810−6918.

(12) Rieger, J.; Stoffelbach, F.; Bui, C.; Alaimo, D.; Jérôme, C.; Charleux, B. Amphiphilic poly (ethylene oxide) macromolecular RAFT agent as a stabilizer and control agent in ab initio batch emulsion polymerization. *Macromolecules* **2008**, *41*, 4065−4068.

(13) Warren, N. J.; Armes, S. P. Polymerization-induced self-assembly of block copolymer nano-objects via RAFT aqueous dispersion polymerization. *J. Am. Chem. Soc.* **2014**, *136*, 10174−10185.

(14) Canning, S. L.; Smith, G. N.; Armes, S. P. A critical appraisal of RAFT-mediated polymerization-induced self-assembly. *Macromolecules* **2016**, *49*, 1985−2001.

(15) Penfold, N. J. W.; Yeow, J.; Boyer, C.; Armes, S. P. Emerging Trends in Polymerization-Induced Self-Assembly. *ACS Macro Lett.* **2019**, *8*, 1029−1054.

(16) Yu, Q.; Ding, Y.; Cao, H.; Lu, X.; Cai, Y. Use of polyion complexation for polymerization-induced self-assembly in water under visible light irradiation at 25 C. *ACS Macro Lett.* **2015**, *4*, 1293−1296.

(17) Ding, Y.; Cai, M.; Cui, Z.; Huang, L.; Wang, L.; Lu, X.; Cai, Y. Synthesis of Low-Dimensional Polyion Complex Nanomaterials via Polymerization-Induced Electrostatic Self-Assembly. *Angew. Chem., Int. Ed.* **2018**, *57*, 1053−1056.

(18) Ding, Y.; Zhao, Q.; Wang, L.; Huang, L.; Liu, Q.; Lu, X.; Cai, Y. Polymerization-Induced Self-Assembly Promoted by Liquid−Liquid Phase Separation. *ACS Macro Lett.* **2019**, *8*, 943−946.
(19) Liu, Q.; Wang, X.; Ma, L.; Yu, K.; Xiong, W.; Lu, X.; Cai, Y. Polymerization-Induced Hierarchical Electrostatic Self-Assembly: Scalable Synthesis of Multicompartment Polyion Complex Micelles and Their Monolayer Colloidal Nanosheets and Nanocages. *ACS Macro Lett.* **2020**, *9*, 454−458.
(20) Zhao, Q.; Liu, Q.; Li, C.; Cao, L.; Ma, L.; Wang, X.; Cai, Y. Noncovalent structural locking of thermoresponsive polyion complex micelles, nanowires, and vesicles via polymerization-induced electrostatic self-assembly using an arginine-like monomer. *Chem. Commun.* **2020**, *56*, 4954−4957.
(21) Klug, A. The tobacco mosaic virus particle: structure and assembly. *Philos. Trans. R. Soc., B* **1999**, *354*, 531−535.
(22) Liang, Y.; Fotiadis, D.; Filipek, S.; Saperstein, D. A.; Palczewski, K.; Engel, A. Organization of the G protein-coupled receptors rhodopsin and opsin in native membranes. *J. Biol. Chem.* **2003**, *278*, 21655−21662.
(23) Kinoshita, M.; Field, C. M.; Coughlin, M. L.; Straight, A. F.; Mitchison, T. J. Self-and actin-templated assembly of mammalian septins. *Dev. Cell* **2002**, *3*, 791−802.
(24) Van Galen, M.; Higler, R.; Sprakel, J. Allosteric pathway selection in templated assembly. *Sci. Adv.* **2019**, *5*, No. eaaw3353.
(25) Voets, I. K.; de Keizer, A.; Cohen Stuart, M. A. Complex coacervate core micelles. *Adv. Colloid Interface Sci.* **2009**, *147−148*, 300−318.
(26) Spruijt, E.; van den Berg, S. A.; Cohen Stuart, M. A.; van der Gucht, J. Direct measurement of the strength of single ionic bonds between hydrated charges. *ACS Nano* **2012**, *6*, 5297−5303.
(27) Bloembergen, N.; Purcell, E. M.; Pound, R. V. Relaxation effects in nuclear magnetic resonance absorption. *Phys. Rev.* **1948**, *73*, 679.
(28) Levitt, M. H. *Spin Dynamics: Basics of Nuclear Magnetic Resonance*; John Wiley & Sons, 2013.
(29) Drache, M.; Schmidt-Naake, G.; Buback, M.; Vana, P. Modeling RAFT polymerization kinetics via Monte Carlo methods: cumyl dithiobenzoate mediated methyl acrylate polymerization. *Polymer* **2005**, *46*, 8483−8493.
(30) van der Kooij, H. M.; Spruijt, E.; Voets, I. K.; Fokkink, R.; Cohen Stuart, M. A.; van der Gucht, J. On the stability and morphology of complex coacervate core micelles: From spherical to wormlike micelles. *Langmuir* **2012**, *28*, 14180−14191.
(31) Nakai, K.; Nishiuchi, M.; Inoue, M.; Ishihara, K.; Sanada, Y.; Sakurai, K.; Yusa, S.-i. Preparation and characterization of polyion complex micelles with phosphobetaine shells. *Langmuir* **2013**, *29*, 9651−9661.
(32) van der Burgh, S.; de Keizer, A.; Cohen Stuart, M. A. Complex coacervation core micelles. Colloidal stability and aggregation mechanism. *Langmuir* **2004**, *20*, 1073−1084.
(33) Amann, M.; Diget, J. S.; Lyngsø, J.; Pedersen, J. S.; Narayanan, T.; Lund, R. Kinetic Pathways for Polyelectrolyte Coacervate Micelle Formation Revealed by Time-Resolved Synchrotron SAXS. *Macromolecules* **2019**, *52*, 8227−8237.
(34) Cohen Stuart, M. A.; Besseling, N. A. M.; Fokkink, R. G. Formation of micelles with complex coacervate cores. *Langmuir* **1998**, *14*, 6846−6849.
(35) Lindhoud, S.; Norde, W.; Cohen Stuart, M. A. Reversibility and relaxation behavior of polyelectrolyte complex micelle formation. *J. Phys. Chem. B* **2009**, *113*, 5431−5439.
(36) Lueckheide, M.; Vieregg, J. R.; Bologna, A. J.; Leon, L.; Tirrell, M. V. Structure−property relationships of oligonucleotide polyelectrolyte complex micelles. *Nano Lett.* **2018**, *18*, 7111−7117.
(37) Pergushov, D. V.; Müller, A. H. E.; Schacher, F. H. Micellar interpolyelectrolyte complexes. *Chem. Soc. Rev.* **2012**, *41*, 6888−6901.
(38) Aguilar, J. A.; Nilsson, M.; Bodenhausen, G.; Morris, G. A. Spin echo NMR spectra without J modulation. *Chem. Commun.* **2012**, *48*, 811−813.

https://dx.doi.org/10.1021/acs.macromol.0c01915
Macromolecules 2020, 53, 10675−10685